
















Spectroscopic Time-series Performance of JWST/NIRSpec from Commissioning Observations

NÉSTOR ESPINOZA ^{1,2} LEONARDO ÚBEDA ¹ STEPHAN M. BIRKMANN ³ PIERRE FERRUIT ⁴ JEFF A. VALENTI ¹
DAVID K. SING ^{5,6} ZAFAR RUSTAMKULOV,⁶ MICHAEL REGAN,¹ SARAH KENDREW,³ ELENA SABBI ¹
EVERETT SCHLAWIN ⁷ THOMAS BEATTY,⁷ LOÏC ALBERT,⁸ THOMAS P. GREENE,⁹ NIKOLAY NIKOLOV,¹ DIANE KARAKLA,¹
CHARLES KEYES,¹ NIMISHA KUMARI ¹⁰ CATARINA ALVES DE OLIVEIRA ⁴ TORSTEN BÖKER ³
MARIA PENA-GUERRERO,¹ GIOVANNA GIARDINO ¹¹ ELENA MANJAVACAS ¹⁰ CHARLES PROFFITT ¹ AND
TIMOTHY RAWLE ³

¹Space Telescope Science Institute, 3700 San Martin Drive, Baltimore, MD 21218, USA

²Department of Physics & Astronomy, Johns Hopkins University, Baltimore, MD 21218, USA

³European Space Agency, c/o STScI, 3700 San Martin Drive, Baltimore, USA

⁴European Space Agency, ESAC, 28692 Villafranca del Castillo, Madrid, Spain

⁵Department of Physics and Astronomy, Johns Hopkins University, Baltimore, MD 21218, USA

⁶Department of Earth & Planetary Sciences, Johns Hopkins University, Baltimore, MD, USA

⁷Steward Observatory, 933 North Cherry Avenue, Tucson, AZ 85721, USA

⁸Institut de recherche sur les exoplanètes and Département de Physique, Université de Montréal, 1375 Avenue Thérèse-Lavoie-Roux, Montréal, QC, H2V 0B3, Canada

⁹NASA Ames Research Center, Space Science and Astrobiology Division, M.S. 245-6, Moffett Field, CA 94035, USA

¹⁰AURA for the European Space Agency, ESA Office, Space Telescope Science Institute, 3700 San Martin Drive, Baltimore, MD, 21218 USA

¹¹ATG Europe for the European Space Agency, ESTEC, Keplerlaan 1, Noordwijk, The Netherlands

(Received; Revised; Accepted)

Submitted to

ABSTRACT

We report on *JWST* commissioning observations of the transiting exoplanet HAT-P-14 b, obtained using the Bright Object Time Series (BOTS) mode of the NIRSpec instrument with the G395H/F290LP grating/filter combination (3 – 5 μ m). While the data were used primarily to verify that the NIRSpec BOTS mode is working as expected, and to enable it for general scientific use, they yield a precise transmission spectrum which we find is featureless down to the precision level of the instrument, consistent with expectations given HAT-P-14 b's small scale-height and hence expected atmospheric features. The exquisite quality and stability of the *JWST/NIRSpec* transit spectrum — almost devoid of any systematic effects — allowed us to obtain median uncertainties of 50-60 ppm in this wavelength range at a resolution of $R = 100$ in a single exposure, which is in excellent agreement with pre-flight expectations and close to the (or at the) photon-noise limit for a $J = 9.094$, F-type star like HAT-P-14. These observations showcase the ability of NIRSpec/BOTS to perform cutting-edge transiting exoplanet atmospheric science, setting the stage for observations and discoveries to be made in Cycle 1 and beyond.

Keywords: exoplanets: transiting exoplanets, atmospheres, instrumentation

1. INTRODUCTION

The NIRSpec/BOTS mode is one of the prime modes for transiting exoplanet science onboard the *James Webb Space Telescope (JWST)* (Beichman et al. 2014; Birkmann et al. 2022). The mode offers precise spectroscopy of transiting exoplanets from 0.6 to 5 μ m in a single exposure via its low resolution ($R \sim 100$) Prism

mode, as well as high resolution (up to $R \sim 2700$) measurements using various combinations of dispersers and filters. As such, the NIRSpec instrument has unique capabilities to cover a wide range of science cases, and is set to perform observations of exoplanets of all sizes and temperature regimes, including worlds that could host suitable conditions for life as we know it (see, e.g., Lewis et al. 2017; Lafreniere 2017; Rathcke et al. 2021; Lim et al. 2021).

During the commissioning of *JWST*, Time Series Observations (TSOs) were obtained in all instruments to determine two key properties of the science instruments and modes. The first was to verify that these technically challenging observations were executing as planned. The second objective was to determine if the various instrument modes could be calibrated with sufficient accuracy to precisely measure the small flux variations caused by the transits, and to identify additional calibration needs if limitations were found.

For the *JWST* instruments offering observations in the near-infrared (NIR; here defined as wavelengths up to $5 \mu\text{m}$), a common target was decided to study the above mentioned properties of TSOs: the transiting exoplanet HAT-P-14 b (Torres et al. 2010). HAT-P-14 b is a dense ($2.3M_J$; $1.15R_J$), short-period (4.6-day) exoplanet orbiting a relatively bright $J = 9.09$, $1.5R_\odot$, low-activity F-star (Bonomo et al. 2017). Given its massive nature, it has a relatively small scale-height ($H \sim 150 \text{ km}$) which, combined with the large stellar radius, should give rise to small variations in the transit depth as a function of wavelength due to the exoplanetary atmosphere (20-60 ppm depending on the assumptions used to calculate this signature). This provided us with an excellent target to commission the NIRSpec/BOTS mode: a target for which we expect, based on reasonable assumptions, a featureless transmission spectrum down to the precision level of the instrument for a single transit. Any observed variations in the transit depth as a function of wavelength therefore would most likely be due to instrumental rather than astrophysical effects, and thus would allow us to pinpoint any irregularities in either the instrument and/or the data reduction and calibration. The HAT-P-14 b system also has the advantage of being thoroughly characterized via precise ground and space-based photometry (see, e.g., Saha & Sengupta 2021; Fukui et al. 2016; Simpson et al. 2011), radial-velocities (e.g., Bonomo et al. 2017; Torres et al. 2010) and even adaptive optics and astrometric constraints on possible nearby companions (Belokurov et al. 2020; Ngo et al. 2015), which enabled us to identify causes for possible deviations from any solutions we

obtained by analyzing *JWST/NIRSpec* spectrophotometry.

Here we present the analysis and results of *JWST* commissioning observations of a single transit event of the exoplanet HAT-P-14 b using the NIRSpec/BOTS mode; the very same data that were used to enable this mode for scientific use. The article is organized as follows. In Section 2, we present the observations and data reduction of the dataset. In Section 3 we present a detailed analysis of the TSO, along with performance metrics for the mode retrieved from these observations. Finally, we conclude with a discussion of our findings in Section 4 and a summary of our main findings in Section 5.

2. OBSERVATIONS AND DATA REDUCTION

2.1. Observations

A TSO was obtained during the *JWST* commissioning campaign on 2022-05-30 between 00:30 and 07:02 UT with the NIRSpec/BOTS mode, targeting the star HAT-P-14 (PID 1118; PI: Proffitt). The objective of this observation was to measure the transit event of the exoplanet HAT-P-14 b in order to measure its transmission spectrum, i.e., the transit depth as a function of wavelength. The 6-hour exposure consisted of 1139 integrations with 20 NRSRAPID groups per integration, taken with the G395H/F290LP grating/filter, which covers the wavelength range from 2.87 to $5.14 \mu\text{m}$ with a resolution of about $R \sim 2,700$, using the S1600A1 aperture and the SUB2048 subarray. This resulted in data gathered by both the NRS1 and NRS2 detectors, each having a height of 32 pixels and a width of 2048 pixels, which included four columns of reference pixels at the left and right edges of the selected subarray. The pixel scale, for reference, is about 100 milli-arcseconds (mas) per pixel.

Figure 1 shows the median rates per integration across the entire exposure, which shows several interesting features. The first and most evident is the clear distorted shape of the spectral trace (blue curve; see Section 2.2 for details on how this was obtained). This covers from 2.7 to 3.7 microns in NRS1, and from about 3.8 to 5 microns on NRS2. The second are a number of bad and hot pixels in the frame. Bad pixel masks are being provided by the NIRSpec team to identify those via the Calibration Reference Data System (CRDS)¹. The third feature is the lack of significant structure in the background, which suggests it will be relatively straightforward to remove it from observations. Finally, we also note what appears to be some scattered light evident on the right-

¹ <https://jwst-crds.stsci.edu/>

most ~ 50 pixels in the NRS1 detector, which is also seen on a few of the left-most pixels of the NRS2 detector. The scale of the count rate in Figure 1 makes this feature appear much more dramatic than it actually is in reality (by design — we wanted to highlight this in the figure): the extra countrate of these enlarged wings only adds of the order of ~ 1 DN/s/pixel, whereas the peak counts in that region are about $\sim 1,000$ DN/s/pixel for HAT-P-14. Even if this component contained scattered light from nearby wavelengths, the resulting dilution of the extracted spectrum would be negligible.

It is important to note that the distortion of the right edge of the spectrum seen in the NRS2 detector made the spectra somewhat hard to extract, as it falls right on the corner of the detector. Based on these commissioning observations, the NIRSpec team therefore decided to move the NRS2 subarray by four pixels in the vertical direction such that the spectrum is fully contained in the subarray, and can be more easily extracted. Therefore, the science observations obtained after commissioning will have a slight offset between the spectral trace seen in NRS1 and NRS2.

2.2. Spectral tracing

We describe the data reduction in detail below, starting from the rates per integration, i.e., the `rateint.fits` products, after reducing the `uncal.fits` files available via the Mikulski Archive for Space Telescopes (MAST²) using version 1.6.2 of the JWST pipeline³ with its default parameters (which we note does not include sky subtraction/calibration for this mode/instrument — we detail how we deal with this in Section 2.3). From these products, we use the `transitspectroscopy` library which contains custom routines designed for transit spectroscopy measurements to reduce the data, which is publicly available via GitHub⁴. First, we independently trace the spectral shape for each integration and for each detector by cross-correlating a Gaussian with each column, and finding the maximum of the resulting cross-correlation function (CCF). For the NRS1 detector, we start this process from column 500 and for the NRS2 detector, we start the process from column 5, in both cases following the trace all the way through the right-edge of the detector. Outliers due to cosmic-rays, bad and hot pixels were identified on these trace shape measurements by running a median filter through the trace at each integration with a window of 11 pixels in the wavelength direction and

finding trace positions deviating more than 5 standard deviations from this trace. The outlier-corrected traces were then smoothed using a spline.

The trace positions as a function of time are presented in Figure 2. These show remarkable stability throughout the exposure, even during a high-gain antenna (HGA) move that happened at about half an hour after the start of the exposure, showing deviations within $1/500$ th of a pixel (0.2 mas) over the 6-hour exposure. There seems to be both high-frequency variations and a slight systematic movement of the trace during the first two hours, but these do not appear to cause any evident systematic trend on the actual spectrophotometry, and seem to be consistent across the two detectors. A detailed analysis of the trace time variability is given in Appendix A.

2.3. $1/f$ corrections

$1/f$ noise is an important component of the near-infrared *JWST* detector noise which can give rise to significant scatter in a TSO if not accounted for and at least partially corrected (see, e.g., Schlawin et al. 2020; Rustamkulov et al. 2022). We perform $1/f$ (and sky background) corrections at the integration level by first masking all pixels within 15 pixels from the traces, and taking the median of the non-masked pixels at each column, subtracting that from each pixel in that column. This methodology is, of course, not perfect because it doesn't take care of the intra-column component of $1/f$ noise; however, it has the added benefit of correcting for any sky background signal, as well as any column-to-column offset created by $1/f$ noise. We find that this correction significantly improves the precision of our analysis, as already suggested by the works of Schlawin et al. (2020) and Rustamkulov et al. (2022).

2.4. Spectral extraction

Using the $1/f$ -corrected integrations and the traces obtained as described in the previous section, we proceed to extract the spectra at each integration. Note this implies we are not flat-fielding our data prior to extraction; the impact of which is presumed to be small given the precise stability of the spectrum presented in the previous sections. Given that we find a number of residual cosmic rays, as well as bad and hot pixels not corrected by the JWST STScI pipeline, we decided to extract the spectrum using the optimal extraction algorithm for distorted spectra of Marsh (1989), which automatically takes care of outliers in the 2D spectral profile. The implementation we use is the one described in Brahm et al. (2017), with the difference that we use a variance array as input to the algorithm.

The spectrum is extracted using a 14-pixel aperture around the trace for NRS1 and NRS2 independently;

² <https://archive.stsci.edu/>

³ <https://github.com/spacetelescope/jwst>

⁴ <https://github.com/nespinoza/transitspectroscopy>

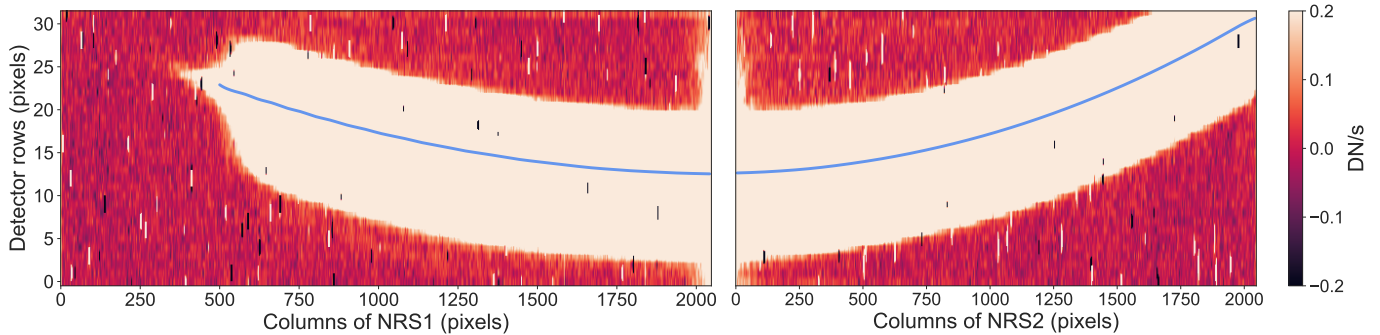


Figure 1. Median signal of all integrations showcasing the 2D spectrum of HAT-P-14 as obtained by NIRSpec/BOTS G395H; the trace of the very first integration as obtained by our methods is shown in blue. These were obtained using the raw rates per integration produced by the JWST pipeline, for which the median background has been subtracted. Hot and bad pixels in the NRS1 and NRS2 detectors are clearly observed, as well as what appears to be some scattered light at the right-edge of NRS1 and left edge of NRS2 (see text for details). Note that the countrate illustrated in the frame is significantly constrained (between -0.2 and 0.2 DN/s) in order to highlight the (minimum) background structure. Also note the aspect ratio of the frame has been stretched in particular in the 32-pixel cross-dispersion direction for illustration purposes.

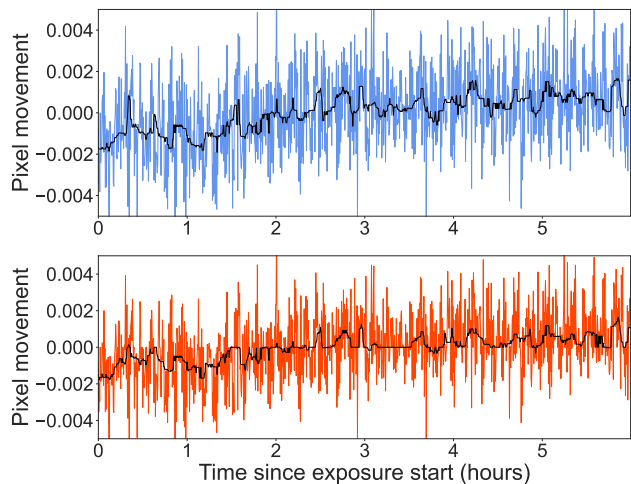


Figure 2. Trace position movement for NRS1 (top, blue) and NRS2 (bottom, red) portions of the spectral trace as a function of time, as tracked by the median movement of all the points in the trace. Black line is a median filter with a window of 11 integrations through the measurements. Note the remarkable stability of the trace position, which stays on the same pixel down to $1/500$ th of a pixel (0.2 mas).

this aperture size was selected as to be consistent across the extracted wavelength range, as well as to be able to maximize the signal-to-noise ratio while being able to extract the spectrum from as a wide wavelength range as possible (other smaller and larger apertures gave overall similar results). For NRS2, we don’t extract the spectrum all the way to the corner; instead, our chosen aperture only allows us to extract the spectrum up to 4.8 microns. Wavelengths are assigned to each column by making use of the JWST pipeline’s wavelength map, which is in turn obtained through the NIRSpec instrument model, which was observed during commission-

ing to work according to pre-flight specifications, which are excellent for the purposes of this work (Lützgendorf et al. 2022). The extracted median spectrum of HAT-P-14 is shown in Figure 3. As can be observed, only a small fraction of the large number of bad and hot pixels clearly seen in Figure 1 remain after using our optimal extraction procedure.

Using these extracted spectra, we then move to a discussion on the analysis and TSO observed performance during commissioning in the next section.

3. TSO ANALYSIS AND PERFORMANCE

3.1. Band-integrated light curve analysis

As a first-order analysis, we construct the “band-integrated” light curve of HAT-P-14 b by adding up the light from NRS1 and NRS2 separately. We decided to fit these light curves with a simple model which included a *batman* transit model (Kreidberg 2015) and a linear trend in time⁵. We used a square-root law to parametrize limb-darkening in these light curve fits as, based on simulations performed by our team similar to those suggested in Espinoza & Jordán (2016), this was one of the laws that performed the best to precisely and accurately recover input transit parameters. As priors for our fit, we used orbital parameters retrieved by fitting *TESS* transit light curves from Sectors 25 and 26 in the exact same manner as described in Patel & Espinoza (2022), from which we obtained $a/R_* = 8.34 \pm 0.31$ and $b = 0.90 \pm 0.02$, and for which we left the eccentricity

⁵ More complex models were tried as well (e.g., a few models including this trend plus a Gaussian Process); however, all of those models were indistinguishable with this simple one judging from the bayesian evidence of our fits ($|\Delta \ln \mathcal{Z}| \lesssim 2$).

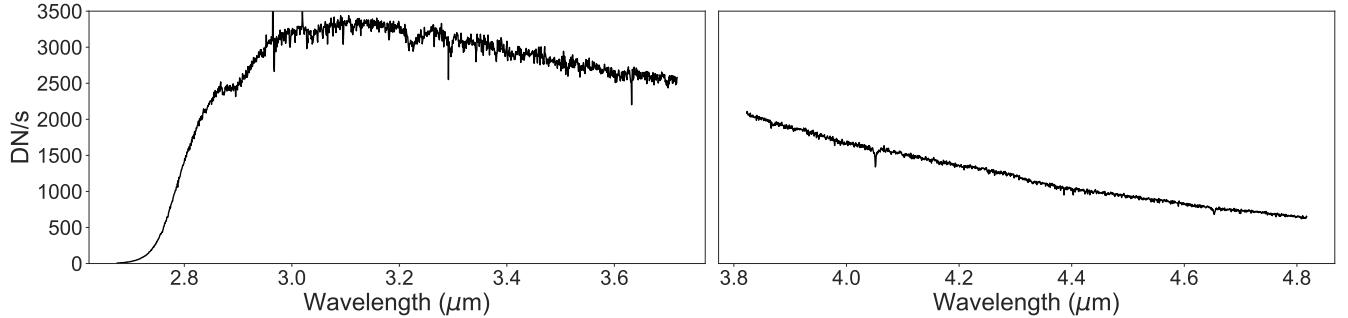


Figure 3. Median extracted spectrum for HAT-P-14 using optimal extraction on the frame shown in Figure 1 for NRS1 (left) and NRS2 (right). Note we only extract up to $4.8 \mu\text{m}$ as the rest of the spectral range up to $5 \mu\text{m}$ falls at the very corner of the detector; this will not be the case for future science observations as the subarray has since been moved by 4 pixels to avoid this (see text for details). Also note the spectra has not been flat fielded, which explains the high frequency variations as a function of wavelength especially in the NRS1 spectrum.

and argument of periastron fixed to the values found in the literature (Bonomo et al. 2017, $e = 0.11$; $\omega = 106.1$ deg) — which we also fixed in our JWST/NIRSpec light curve fits. Finally, we used the parametrization of Kipping (2013) in our band-integrated light curve fits, leaving the transformed limb-darkening coefficients (q_1, q_2) as free parameters in our fits with uniform priors between 0 and 1. A jitter term was also added and fitted to both light curves. The juliet (Espinoza et al. 2019) library was used to perform these light curve fits independently for NRS1 and NRS2, using dynesty as the sampler via dynamic nested sampling (Speagle 2020). The results of those fits are presented in Figure 4; a Table with our priors and posteriors is presented in Table 1.

As can be observed, the simple model defined above resulted in an excellent fit to our JWST/NIRSpec G395H data. This is quite impressive, considering we did not remove any data points for the fit, in particular data points at the beginning of the exposure. This suggests that there are negligible persistence effects in the NRS1 and NRS2 detectors, at least at the fluences probed by our observations. The observed scatter in the light curve, however, is larger than expected from pure read-noise and photon-noise statistics as calculated by the JWST pipeline by a factor of about 3; the most likely explanation for this is residual $1/f$ spatial covariance which causes extra white-noise scatter in a TSO — noise that is not seen nor impacts the analyses if one performs light curve analyses at the resolution level of the instrument (see Section 3.2 for a discussion on this), where we reach photon and read-noise limited precision. Indeed, the overall residual structure of a simple light curve fit like this shows a lack of correlated noise structure. We demonstrate this using Allan variance plots on

the residuals, presented in Figure 5. The plots show that as we bin the data in time, the standard deviation decreases closely following a $1/\sqrt{N_{bin}}$ shape (dashed lines in this figure), which is consistent with the expectation for uncorrelated white-noise.

It is interesting to note, however, that the NRS1 transit light curve clearly shows a more pronounced exposure-long slope than the NRS2 one (about -140 ppm per hour for NRS1, compared to 40 ppm per hour for NRS2). While we observe some wavelength-dependence of the slope for NRS1 (see next sub-section), the smaller slope seen in the NRS2 light curves is fairly constant for all wavelengths. Given that the NRS1 fluence levels vary relatively little at the high signal-to-noise ratio portions of the spectra as compared to NRS2 (see Figure 1), it is unlikely this is purely a fluence-dependent effect. Also, given the significant difference between the slopes on NRS1 and NRS2, it is unlikely this is, e.g., an astrophysical, observatory (e.g., “tilt” events; Rigby et al. 2022) and/or instrument-level effect — all those explanations should give rise to smooth transitions from one detector to the other as well as similar effects on both detectors. The latter two set of hypotheses are also unlikely given the stability of both the traces (Figure 2) and the full-width at half maximum (FWHM; a detailed analysis of the FWHM shape and its time stability is presented in Appendixes A and B) of the spectral profile measured during the observations, which we present on Figure 6 and which have been shown by Schlawin et al. (in prep.) and Beatty et al. (in. prep.) to be excellent tracers of “tilt events”. Given all this, it is possible the effect is due to some underlying detector-level effect, but this is currently under investigation. A discussion on possible causes is presented in Section 4.

3.2. Wavelength-dependent light curve analysis

Table 1. Prior and posterior parameters of the band-integrated lightcurve fits performed on the NRS1 and NRS2 data of HAT-P-14 b. For the priors, $N(\mu, \sigma^2)$ stands for a normal distribution with mean μ and variance σ^2 ; $U(a, b)$ stands for a uniform distribution between a and b , respectively and $\log U(a, b)$ stands for a log-uniform prior on the same ranges. Priors for b and a/R_* come from *TESS* (see text for details).

Parameter	Prior	Posterior (NRS1)	Posterior (NRS2)	Posterior (combined)
<i>Physical & orbital parameters</i>				
P (days)	4.62767 (fixed)			
t_0 (BJD TDB)	$N(2459729.71, 0.2^2)$	$2459729.70662^{+0.00010}_{-0.00010}$	$2459729.70696^{+0.00016}_{-0.00017}$	$2459729.706791^{+0.000094}_{-0.000093}$
R_p/R_*^ψ	$U(0.0, 0.2)$	$0.0826^{+0.0020}_{-0.0014}$	$0.0849^{+0.0022}_{-0.0018}$	$0.0839^{+0.0014}_{-0.0012}$
$b = (a/R_*) \cos(i)$	$N(0.90, 0.02^2)$	$0.9081^{+0.0049}_{-0.010}$	$0.8966^{+0.0068}_{-0.0084}$	$0.9016^{+0.0048}_{-0.0060}$
a/R_*	$N(8.34, 0.31^2)$	$8.29^{+0.18}_{-0.11}$	$8.40^{+0.17}_{-0.15}$	$8.354^{+0.12}_{-0.098}$
e	fixed	0.11	0.11	
ω	fixed	106.1	106.1	
<i>Limb-darkening coefficients</i>				
q_1^\dagger	$U(0, 1)$	$0.14^{+0.41}_{-0.11}$	$0.49^{+0.29}_{-0.28}$	
q_2^\dagger	$U(0, 1)$	$0.58^{+0.30}_{-0.40}$	$0.58^{+0.28}_{-0.34}$	
<i>Instrumental parameters</i>				
M_{flux} (ppm)	$U(0, 10^5)$	313^{+13}_{-13}	-77^{+21}_{-22}	
θ_0^\ddagger (ppm)	$U(-10, 10)$	-258^{+11}_{-10}	66^{+18}_{-18}	
σ_w (ppm)	$\log U(10, 10^4)$	$336.8^{+7.4}_{-7.8}$	$534.8^{+12.4}_{-11.8}$	

^{ψ} For a more precise estimate on the transit depth, see Figure 11. See text for an explanation of why the band-integrated light curve achieves lower precisions than the light curves at each resolution element sampled by the instrument.

^{\dagger} These parameterize the square-root limb-darkening law using the transformations in Kipping (2013).

^{\ddagger} The linear trend slope was fitted to the standardized times, i.e., to the mean-subtracted time-stamps divided by the standard deviation of the time-stamps.

3.2.1. Light curve scatter

Before jumping into the analysis of the transit event as a function of wavelength, we perform simple analyses to understand whether the light curve scatter at the native resolution of the instrument is, indeed, being correctly estimated by the JWST pipeline. This latter calculation includes both photon-noise and read-noise characteristics of the detector, including the impact of 1/f noise on a single pixel, but not the covariance this might have with nearby pixels.

To perform this comparison, we took the out-of-transit scatter (i.e., the standard deviation of the flux time-series) on the wavelength-dependant light curves of both NRS1 and NRS2 at the spectral sampling of the instrument (i.e., at each column in Figure 1) and compared that to the out-of-transit median errorbars reported by the JWST pipeline (i.e., adding in quadrature the pipeline-reported uncertainties on a given column, and taking its square-root). We then simply took the ratio of these two numbers, which in an ideal world should be exactly 1. These ratios are presented in Figure 7.

As can be seen from Figure 7, at the native resolution of the instrument, the JWST pipeline precisely predicts the noise levels observed on the out-of-transit light curves. There seems to be, however, a slight but significant extra scatter of about 5% in the actual data when compared against the pipeline products for NRS2. The source of this discrepancy is currently under investigation.

Next, we perform the same analyses but performing *binning* of the spectral channels. This is a somewhat standard procedure in transiting exoplanet spectroscopy for which combining the light from different wavelength bins (i.e., columns in Figure 1) helps to boost the signal-to-noise ratio of the light curves, with the band-integrated light curves in Section 3.1 representing the limiting case for this approach. The motivation for doing such an experiment on *JWST* data is 1/f noise. While we performed some corrections on this effect in Section 2.3, these are most definitely not correcting the effect completely. Column-by-column median subtraction, in particular, can be roughly thought of as subtracting the median every 32 samples of a 1/f time-series.

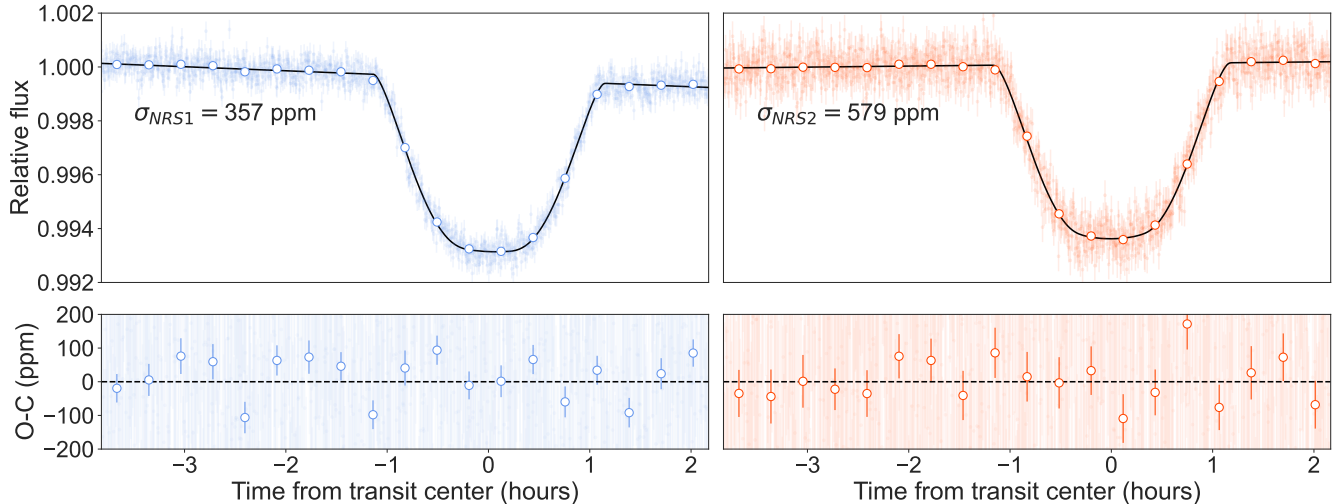


Figure 4. band-integrated transit light curves for HAT-P-14 b as observed by NIRSpec/BOTS G395H via the NRS1 (left) and NRS2 (right) detectors. These have been fitted simply by a transit model and a linear trend, which seems to be sufficient to match the variations observed in the data. Note the quoted precision is at a cadence of 19 seconds after fitting.

This will procedure thus will remove some but not all the covariance both within and between columns in a given integration. Hence, some residual covariance due to $1/f$ noise is expected to “leak” into our measurements.

Figure 8 shows the same experiment as Figure 7, but after performing spectral binning after spectral extraction of three different widths: 10, 30 and 100 columns/pixels for NRS1 (as a comparison, the band-integrated light curve for NRS1 implies a 1543-column bin). The results of this experiment shows that one observes a larger scatter than the one one would expect by simply adding in quadrature the uncertainties reported by the JWST pipeline. We believe part of this is related to the residual covariance between pixels of different columns described above, which makes our simple addition-of-variances to estimate the resulting noise of the bin a lower limit on the actual total variance. Part of it could also be instrumental systematics that only become evident once a better signal-to-noise ratio is attained via the spectral binning. A full investigation and implementation of the covariance due to, e.g., $1/f$ noise on the JWST pipeline is outside the scope of this work (but see, e.g., Schlawin et al. 2020), as well as a detailed investigation of more subtle sources of systematic noise. Despite of this, in our experiments we have found that the best way to work with *JWST* data from NIR detectors is to work at the spectral sampling level of the instrument (i.e., at the column-to-column level). Then, observables such as, e.g., the transit depth as a function of wavelength can be binned in a post-processing stage. We have found this methodology to give the most accurate and precise results during commissioning.

3.2.2. Wavelength-dependent light curve modelling

Following the procedures described above, we proceeded to model the wavelength-dependant light curves in the very same way as described for the band-integrated light curve in Section 3.1. The only difference was that we (1) fixed the orbital parameters to the same ones ingested as priors on the band-integrated lightcurve analysis, (2) fixed the time-of-transit center to the one found in our band-integrated lightcurve analysis and (3) used priors on the square-root limb-darkening coefficients instead of letting them go free in the light curve fitting procedure. The prior was a truncated Gaussian defined between 0 and 1 for both q_1 and q_2 ; the mean of those Gaussians was obtained by using the `limb-darkening` package described in Espinoza & Jordán (2015), for which we ingested the stellar properties of HAT-P-14 defined in Bonomo et al. (2017) and used ATLAS (Kurucz 1979) intensity profiles to compute model limb-darkening coefficients. Then, we passed the resulting non-linear limb-darkening coefficients through the SPAM algorithm of Howarth (2011) to obtain the final square-root law limb-darkening coefficients we set for the mean of our priors. The standard deviation of the prior for each coefficient was set to 0.1. Following the lessons learned in Section 3.2.1, we work at the resolution level of the instrument and fit each transit light curve with a combination of a transit model and a slope, which we found gave very good results.

Figure 9 show some sample light curves fitted following our procedures. As can be seen, the quality of these native-resolution light curves is very good, and our transit model plus linear trend seems to be enough to model most of the systematic trends observed in the data.

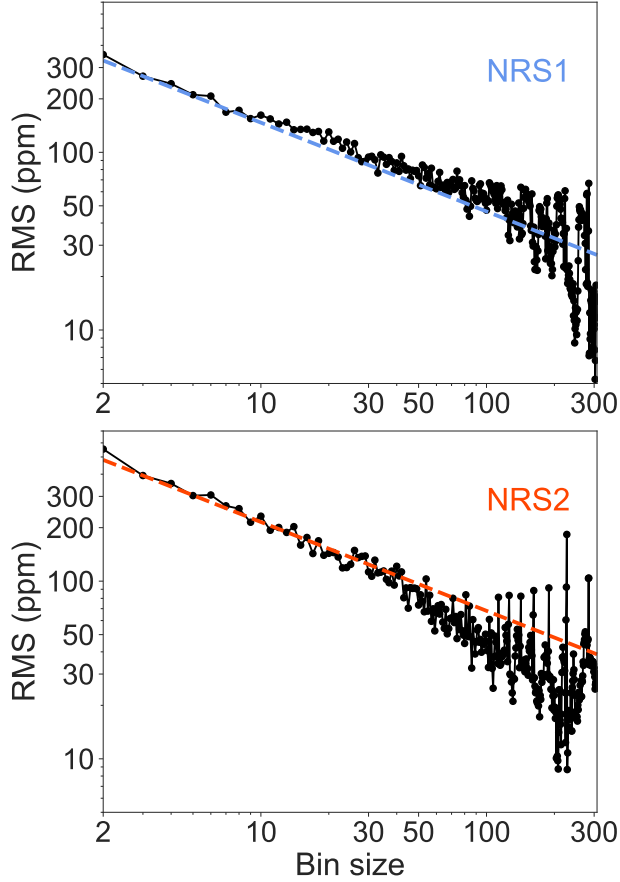


Figure 5. Allan Variance plots for the band-integrated light curve fits residuals shown in Figure 4 for NRS1 (top) and NRS2 (bottom). Dashed colored lines show the expected decrease on the scatters as a function of binning for perfect white-noise, i.e., decreasing as the square-root of the bin-size, which is a very good match to the actual observed data, suggesting a lack of strong correlated noise structure.

Our wavelength-dependant transits allowed us to measure two observables. First, it allowed us to explore the wavelength-dependence of the exposure-long linear trends already described in Section 3.1, but it also allowed us to obtain the main observable used to commission the instrument: the transit depth (and its uncertainty) as a function of wavelength. We discuss our analyses of those two observables in the next sub-sections.

3.2.3. Linear trend wavelength dependence

From our light curve modelling described in Sections 3.1 and 3.2.2, we were able to retrieve the wavelength-dependence of the linear trend observed both in the NRS1 and NRS2 data. While we obtained these slopes at the resolution element of the instrument, we bin those down to a resolution of $R = 200$ for easier visualization. Figure 10 show the slopes as a function of wavelength

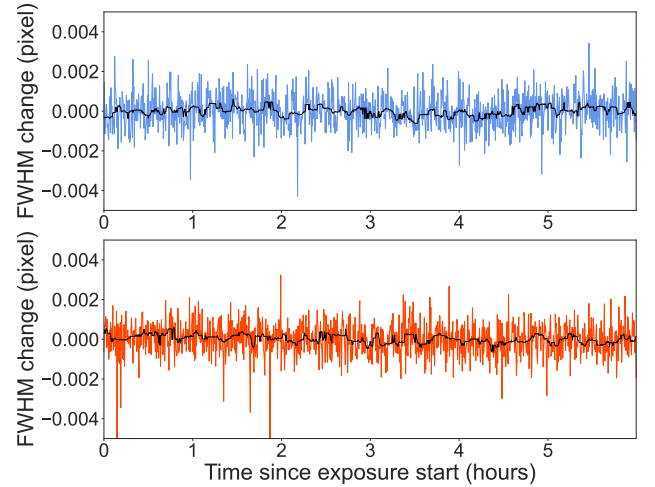


Figure 6. FWHM change over the course of the exposure for NRS1 (top, blue) and NRS2 (bottom, red) portions of the spectral trace. Black line is a median filter with a window of 21 points through the measurements. Note the remarkable stability of the FWHM over the course of the observations — it stays stable to about 1/1000th of a pixel.

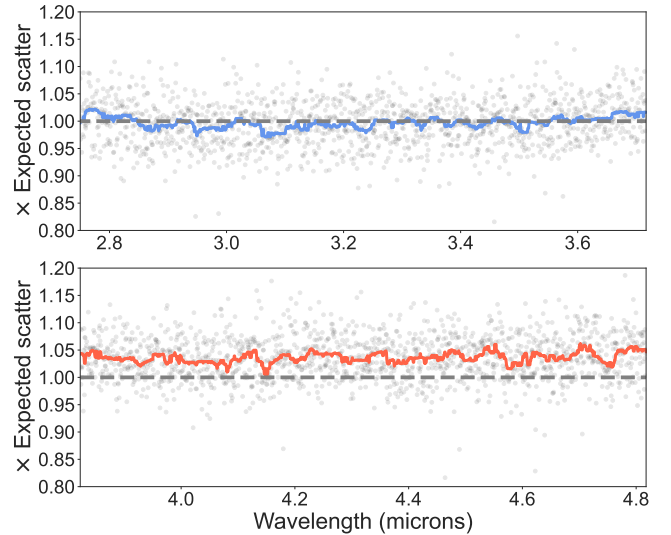


Figure 7. Ratio between measured over expected (from the JWST pipeline) out-of-transit light curve scatter for our HAT-P-14 TSO as seen by NRS1 (top) and NRS2 (bottom). Note how the pipeline precisely predicts the observed scatter for NRS1, whereas for NRS2 there is a slight extra scatter at the 5% level. Colored lines show median filters for easier visualization; grey dashed lines represent the ideal value of 1.

for both NRS1 and NRS2. As can be observed, a slope is observed in both detectors, but the observed slope is much stronger on NRS1 than in NRS2 as already hinted in Section 3.1.

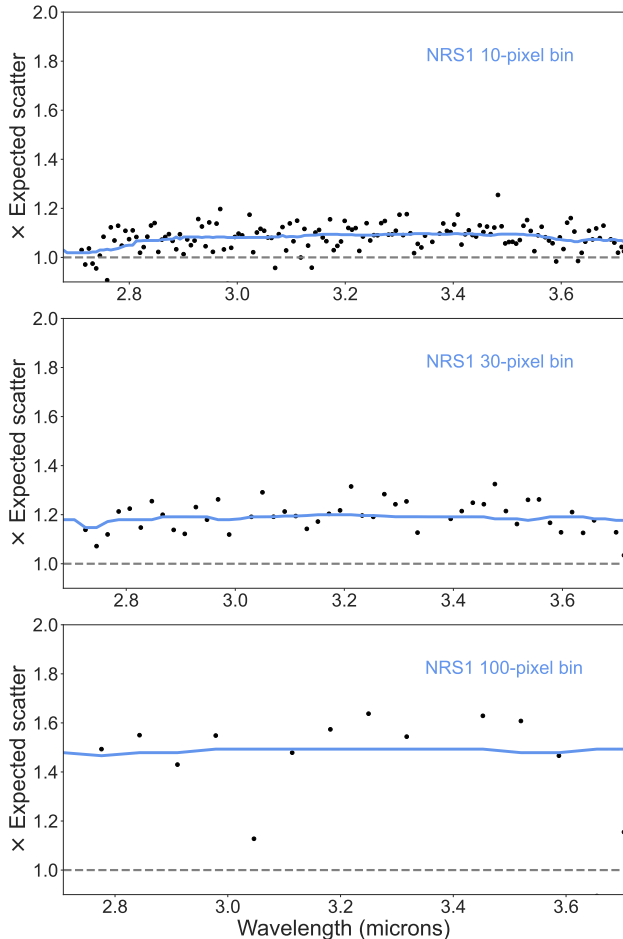


Figure 8. Ratio between measured over expected (from the JWST pipeline) out-of-transit light curve scatter for our HAT-P-14 TSO as seen by NRS1 using different number of spectral bins: 10 (top), 30 (middle) and 100 pixels/elements (bottom) panels (black points; blue lines are median filters shown for illustration). As can be seen, the larger the bin, the larger the deviation of the observed scatter versus the predicted one just from the JWST pipeline error bars. The main suspect for this behavior is $1/f$ noise (see text).

Our results for the wavelength-dependence of the exposure-long slope are very interesting in particular for NRS1. First, it seems at the shortest wavelengths of the NRS1 data the slope strongly decreases in amplitude down to around zero. However, it quickly settles to a value of about -140 ppm/hour at about 3 microns, and stays more or less constant at the redder NRS1 wavelengths. The constant value observed for the NRS2 detector, however, is of about 30 ppm/hour — a factor of almost 5 smaller in amplitude (and different sign). Given the completely different level of slopes observed between the detectors, the stability of other metrics (e.g., trace positions, FWHM), and the fact that the amplitude and sign of the slopes don’t smoothly evolve

Table 2. Transmission spectrum of HAT-P-14 b (at $R = 100$) as measured by our NIRSpec/BOTS G395H observations.

Wavelength (μm)	Transit Depth (ppm)	Error (ppm)
2.771	6592	110
2.800	6710	74
2.829	6682	72
2.859	6696	49
2.888	6620	36
2.918	6750	66
2.948	6671	53
2.979	6599	43
3.010	6590	55
...
4.526	6695	66
4.572	6653	67
4.619	6691	74
4.667	6602	72
4.715	6591	78
4.763	6573	81

NOTE— A sample of the dataset is shown here. The entirety of this table is available in a machine-readable form in the online journal.

as a function of wavelength from one detector to the other as a function of wavelength, there is a strong suggestion that the slope is somehow introduced at the detector level in the NRS1 detector. We further discuss this possibility in Section 4.

3.2.4. HAT-P-14 b’s transmission spectrum

Next, we retrieve HAT-P-14b’s transmission spectrum from our light curve fits. As discussed above, the transmission spectrum we forge is obtained at the resolution level of the instrument, which we then bin down to a lower resolution of $R = 100$. Figure 11 (and Table 2) shows the transmission spectrum of HAT-P-14 b. To test whether this spectrum is consistent with a featureless spectrum (which is the expectation), we performed a chi-square test under the assumption of a flat spectrum and found a p-value of 0.13 — consistent with the featureless spectrum scenario. Running the test separately on NRS1 and NRS2 yielded p-values of 0.11 and

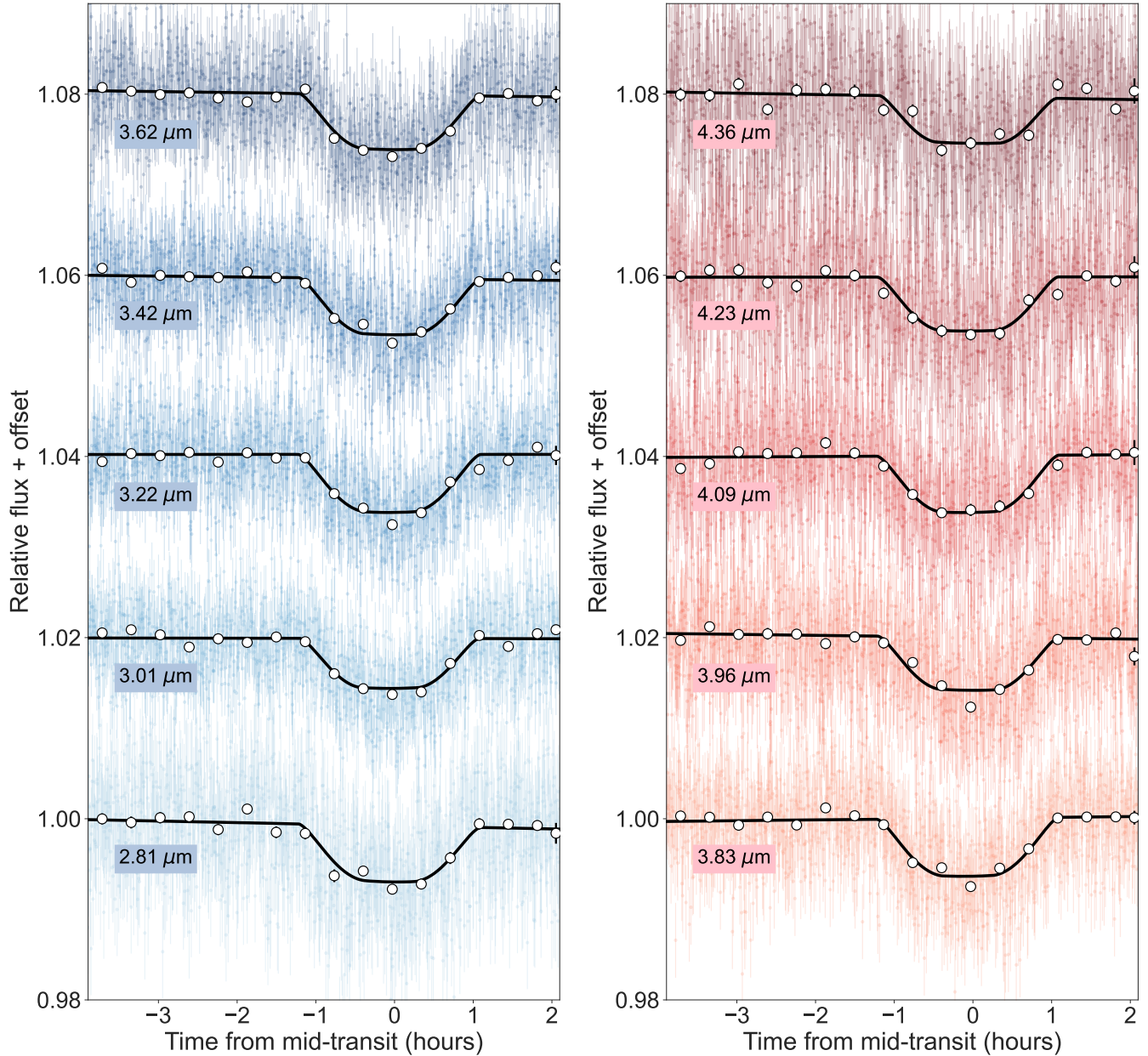


Figure 9. Sample, unbinned wavelength-dependant transits of HAT-P-14 b obtained in our commissioning NIRSpect/BOTS G395H observations for NRS1 (blue, left plot) and NRS2 (red, right plot). The black solid lines show our transit plus systematic model; white points are 70-integration bins shown for illustration purposes.

0.30, respectively — also consistent with the featureless spectrum scenario. It is also important to note that all data points above $2.85 \mu\text{m}$ at $R = 100$ have uncertainties below 100 ppm — in particular, the median error bar of the spectrum on NRS1 at those wavelengths is 48 ppm, with the scatter on the spectrum itself being 48 ppm (i.e., both consistent with each other). Similarly, for NRS2, the median uncertainties were of 63 ppm with an actual measured standard deviation on the spectrum of 64 ppm (again, both consistent with each other). As we will show in Section 4, while these precisions are

about 20% larger than what tools like PandExo (Batalha et al. 2017) predict, they are about $\sim 10\%$ better than pre-flight expectations from Pandemia (Pontoppidan et al. 2016) if one accounts for the fact that we are fitting for a limb-darkened star and not a flat-bottomed transit as the one PandExo assumes.

One final notable result from this transit spectrum is the exquisite precision on the broadband transit depth we are able to obtain by calculating the weighted mean of the transit depth at all wavelengths using this transit spectrum: we obtain a weighted mean transit depth

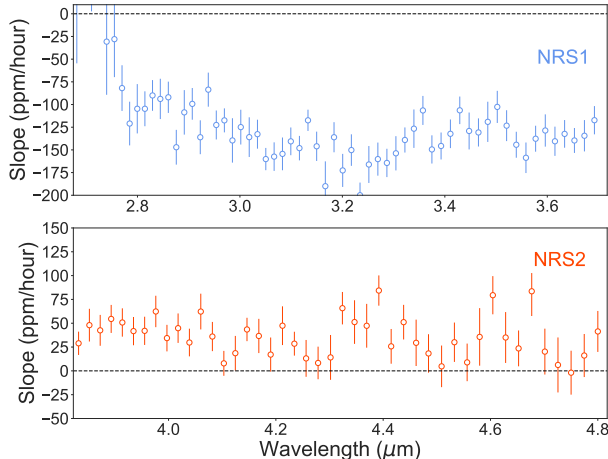


Figure 10. Exposure-long slopes observed in our NIRSpec/BOTS observations for both NRS1 (top) and NRS2 (bottom) in ppm per hour as a function of wavelength. Dashed line indicates a no-slope scenario in both cases. Note the different values of the slopes between the two cases: negative decreasing to lower values as wavelength increases for NRS1; mostly constant positive value for NRS2. No smooth transition is seen as a function of wavelength, which suggests this is a detector-level systematic.

of 6627 ± 8 ppm (purple band in Figure 11), which is in excellent agreement (within 1-sigma) of the one obtained by the *JWST/NIRCam* short-wavelength photometry observations of HAT-P-14 b (Schlawin et al., in prep.).

4. DISCUSSION

4.1. General TSO performance of NIRSpec/BOTS

Via a detailed analysis of the TSO targeting a transit event of the exoplanet HAT-P-14 b, we have shown in Section 3 the excellent sensitivity and stability of NIRSpec/BOTS to perform precise relative flux measurements, successfully enabling us to understand the two key properties we set as objectives for our commissioning observations: that the instrument is properly working for these kind of scientific objectives and that, indeed, the instrument can be calibrated to perform these precise flux measurements.

The fact that the instrument is properly working for precise flux measurements was shown at several stages. In particular, perhaps the most straightforward is that, as shown in Section 3.2 and Figure 11, we are able to obtain a featureless transmission spectrum of the exoplanet HAT-P-14 b, which was the expectation given its massive nature. In addition, the precision with which we measure this spectrum (transit depth errors of 50-60 ppm at a resolution of $R = 100$) is very close to what was expected prior to launch. We compare our results

to pre-flight expectations in Figure 12 via two experiments. The first was to compare the transit depth errors we obtain against predictions from PandExo (Batalha et al. 2017, grey points in Figure 12), from which we observe precisions that are about $\sim 20\%$ larger than those simulations. One important caveat of PandExo, however, is that the tool assumes flat-bottomed transits to perform its transit depth calculations, i.e., it omits the impact of limb-darkening in the transit lightcurves. While in general at the wavelengths probed by our NIRSpec/G395H observations this assumption might be a fair one to make, the limb-darkening effect on the transit lightcurve is very prominent on HAT-P-14 b due to the relatively large impact parameter of the transits (see Table 1). This can be readily observed in the “U”-shaped transit lightcurve both in Figures 4 and 9. In order to perform an “apples-to-apples” comparison to pre-flight expectations then, on our second experiment we decided to use the input noise information from Pandeia (Pontoppidan et al. 2016) that PandExo uses to generate its simulations to produce noisy limb-darkened transit lightcurves instead. These simulated transit lightcurves had limb-darkening profiles assuming a non-linear limb-darkening law, with coefficients calculated as described in Section 3.2 and generated using *batman* (Kreidberg 2015). After simulating them at all the resolution elements sampled by NIRSpec/G395H, these were fitted in the exact same manner as we fitted our real transit lightcurves already described in Section 3.2 and the resulting transit depths were binned down to $R = 100$. The resulting transit depth errors from that experiment — depicted as blue points in Figure 12 — show that our actual NIRSpec/G395H precisions are *better* by about $\sim 10\%$ than pre-flight expectations.

The fact that our results are better than pre-flight expectations in the transit spectrum is interesting but within expectations given the better-than-expected throughput of the *JWST* NIRSpec/G395H configuration (Giardino et al. 2022). Furthermore, as the above experiments and the ones shown in Section 3.2.1 show, we believe we are very close (if not *at*) the “photon-noise” (plus read-noise) limit, given how precisely the *JWST* pipeline predicts the actual lightcurve scatter at the resolution elements sampled by the instrument.

4.2. Lightcurve systematics

As it was shown in Sections 2 and 3, the second objective of our TSO observations — to confirm that the instrument can be calibrated to perform precise relative flux measurements as the ones needed for transiting exoplanet observations — has been readily met, with the level of systematic effects on the TSO itself being very

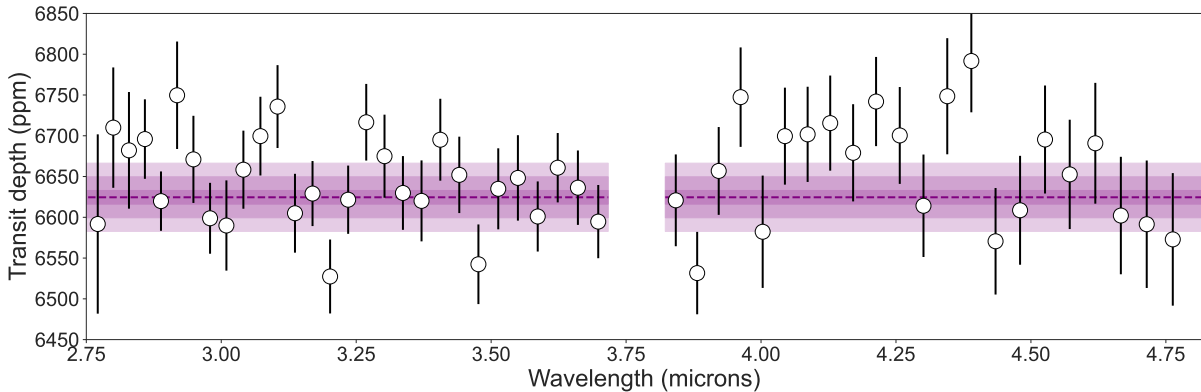


Figure 11. Transmission spectrum for HAT-P-14 b as obtained by our NIRSpec/BOTS G395H observations. The high-resolution spectrum has been binned to a resolution of $R = 100$ from 2.7 to 4.8 μm (white points with error bars); the weighted mean transit depth across the bandpass is 6627 ± 8 ppm (purple line with bands denoting 1, 3 and 5 sigma bands around this value). The gap in the middle, at about 3.75 μm , is due to the detector gap between NRS1 and NRS2 also seen in Figures 1 and 3. The spectrum is featureless (p -value > 0.1), as expected for a massive exoplanet like HAT-P-14 b, down to the precision at which we measure the transit spectrum, which is of 50-60 ppm at this resolution (see Table 2).

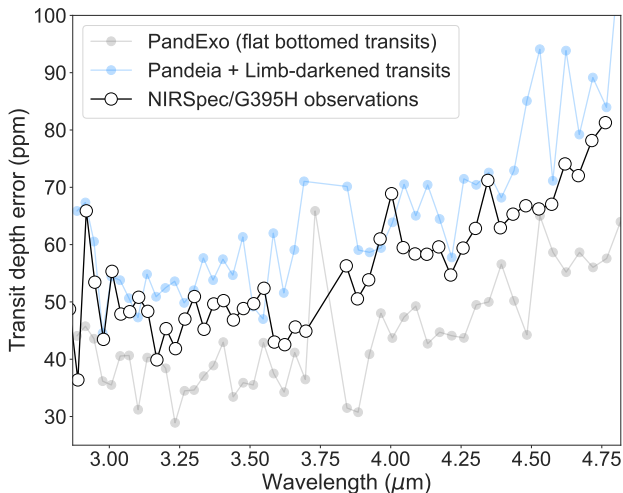


Figure 12. Observed error on the transit depth at $R = 100$ as a function of wavelength from our NIRSpec/G395H observations (Figure 11 & Table 2; white points) against pre-flight predictions from PandExo (grey points) and a simulation using Pandeia plus a limb-darkened transit (blue curve), a better “apples-to-apples” comparison to our observations. Our observations are about 10% better than these latter simulations.

small. However, as it was shown in Section 3, the NRS1 detector seems to show an exposure-long slope which had no straightforward explanation. While it seems this might be a detector-level effect, it’s unclear what step and/or calibration could be producing it. A superbias, background and/or dark-current-related effect, for instance, would cause a source of dilution at the precision level of the transit spectrum, but it would be hard for it to produce and/or significantly change the amplitude

of an exposure-long slope. A linearity problem could, in theory, amplify an existing trend in the data as well (e.g., the trend observed in the NRS2 detector); however, below 2.9 μm and above about 3.6 μm , NRS1 has a very similar fluence level to that observed in NRS2. Looking at Figure 10, it is unlikely thus that this could be the effect producing the differences. In addition, an amplification and/or dilution source like the ones discussed would also imply the same impact on the transit spectrum; however, we don’t see a significant difference between the transit spectrum obtained between NRS1 and NRS2 in Figure 11. One possibility under study involves the fact that internal flat calibrations were performed up to two hours before the TSO exposure presented in this work. This could have filled some detector traps akin to those observed in, e.g., *HST/WFC3* (Zhou et al. 2017) in NRS1 which are slowly being released during the TSO. This, however, does not directly explain why the observed slope in NRS1 is so different from that of NRS2, despite the fact they are very similar detectors (with a gain difference of only about 10%). A possibility is that while these detectors are of the same family, they do have, indeed, different inherent properties like e.g., responses to charge trapping and/or persistence. Other datasets obtained both with this mode and NIRSpec/Prism should be investigated in detail to search for the repeatability of the slopes and the corresponding amplitudes observed in our HAT-P-14 b observations.

4.3. Timing accuracy of JWST time-stamps

As shown in Section 3.1 and presented in Table 1, our observations allowed us to obtain a precise combined time-of-transit between NRS1 and NRS2 of

2459729.706791 $^{+0.000094}_{-0.000093}$ BJD TDB — an uncertainty on the timing of the event of only 8 seconds. While from the lessons learned in Section 3.2 an even better precision is achievable on this timing if the lightcurve analyses are performed at the resolution level of the instrument, this timing precision is enough to test the accuracy of the observatory time-stamps at the tens of seconds accuracy, at least as compared to another mission: *TESS*. Additional data to the one used in Section 3.1 was recently released by the *TESS* mission for HAT-P-14 b for sectors 52 and 53 which include a *contemporaneous* transit to that observed by our *JWST/NIRSpec* observations presented in this work. Using the same methods as presented in Patel & Espinoza (2022), we performed a joint fit of all the 2-minute cadence photometry from *TESS*, including Sectors 25, 26, 52 and 53. We retrieve transit parameters from those *TESS* observations consistent with those presented in Section 3.1 and Table 1, and obtain a transit ephemerides of $P = 4.6276618 \pm 0.0000018$ days and $t_0 = 2459766.72798 \pm 0.00020$ (BJD TDB). In particular, for the transit event observed by *JWST/NIRSpec*, the *TESS* observations observe a time-of-transit of $2459803.74927 \pm 0.00022$ BJD TDB, which is in excellent agreement with the timing of our *JWST/NIRSpec* observations — the difference between the two being 9 ± 19 seconds — consistent with zero at $1\text{-}\sigma$.

5. SUMMARY

We have presented spectrophotometric TSO commissioning observations of HAT-P-14 b using NIRSpec/BOTS onboard *JWST*, which we used to enable the mode for scientific usage. We measured a transmission spectrum of the exoplanet down to a precision of 50-60 ppm at $R = 100$, showcasing in turn the excellent stability and sensitivity of this instrument/mode to perform precise transiting exoplanet spectrophotometry.

We find the above quoted precisions are, in turn, very close to pre-flight expectations. When compared against PandExo, these precisions seem to be about 20% larger than what the tool predicts, but we find most if not all of this difference is due to the assumption of a flat-bottomed transit lightcurve by the tool. If we instead simulate limb-darkened transit lightcurves using the pre-flight noise expectations from Pandeia (which is the engine both PandExo and the *JWST* Exposure Time Calculator⁶ itself uses), we find the observed transit depth errors are about 10% better than those simulations.

While the trace position and FWHM remained fairly constant during our observations —down to 1/500th and 1/1000th of a pixel, respectively — we did find a low-amplitude exposure-long slope on the two detectors used to capture the spectra of HAT-P-14. In particular, the slope observed in NRS1 is much stronger and wavelength-dependent than the one observed in NRS2, and all evidence points to it being a detector-level effect. Investigations to understand this trend are currently ongoing.

Through a series of experiments, we also found that 1/f detector noise, as expected from pre-flight experiments (Schlawin et al. 2020; Rustamkulov et al. 2022), seems to be an important component to pay attention to when studying *JWST* TSOs with NIRSpec/BOTS. In particular, it seems binning spectral channels causes a degradation on the signal-to-noise ratio that might be in part caused by the residual covariance this detector effect ingests into the lightcurves when binning. We found that the best way to work with *JWST* data from NIR detectors such as the ones in NIRSpec/BOTS is to work at the spectral sampling level of the instrument (i.e., at the column-to-column level). Then, observables such as, e.g., the transit depth as a function of wavelength can be binned in a post-processing stage. This methodology gave the most accurate and precise results during our commissioning analyses.

We conclude that the two main objectives of these NIRSpec/BOTS TSOs have been met: our analysis shows that the instrument is properly working to measure the precise relative flux measurements implied by the technique of transit spectroscopy, and that indeed, the instrument can be calibrated to perform these precise measurements. *JWST* NIRSpec is thus ready to perform cutting edge exoplanetary science for Cycle 1 and beyond.

¹ All figures were prepared using Python 3.8.13 with
² the aid of packages matplotlib 3.5.2, NumPy 1.22.4,
³ SciPy 1.8.1 and juliet 2.2.0. This work is based
⁴ on observations made with the NASA/ESA/CSA James
⁵ Webb Space Telescope. The data were obtained from
⁶ the Mikulski Archive for Space Telescopes at the Space
⁷ Telescope Science Institute, which is operated by the As-
⁸ sociation of Universities for Research in Astronomy, Inc.,
⁹ under NASA contract NAS 5-03127 for *JWST*. These
¹⁰ observations are associated with program #01118. This
¹¹ paper includes data collected by the *TESS* mission.
¹² Funding for the *TESS* mission is provided by the
¹³ NASA’s Science Mission Directorate.

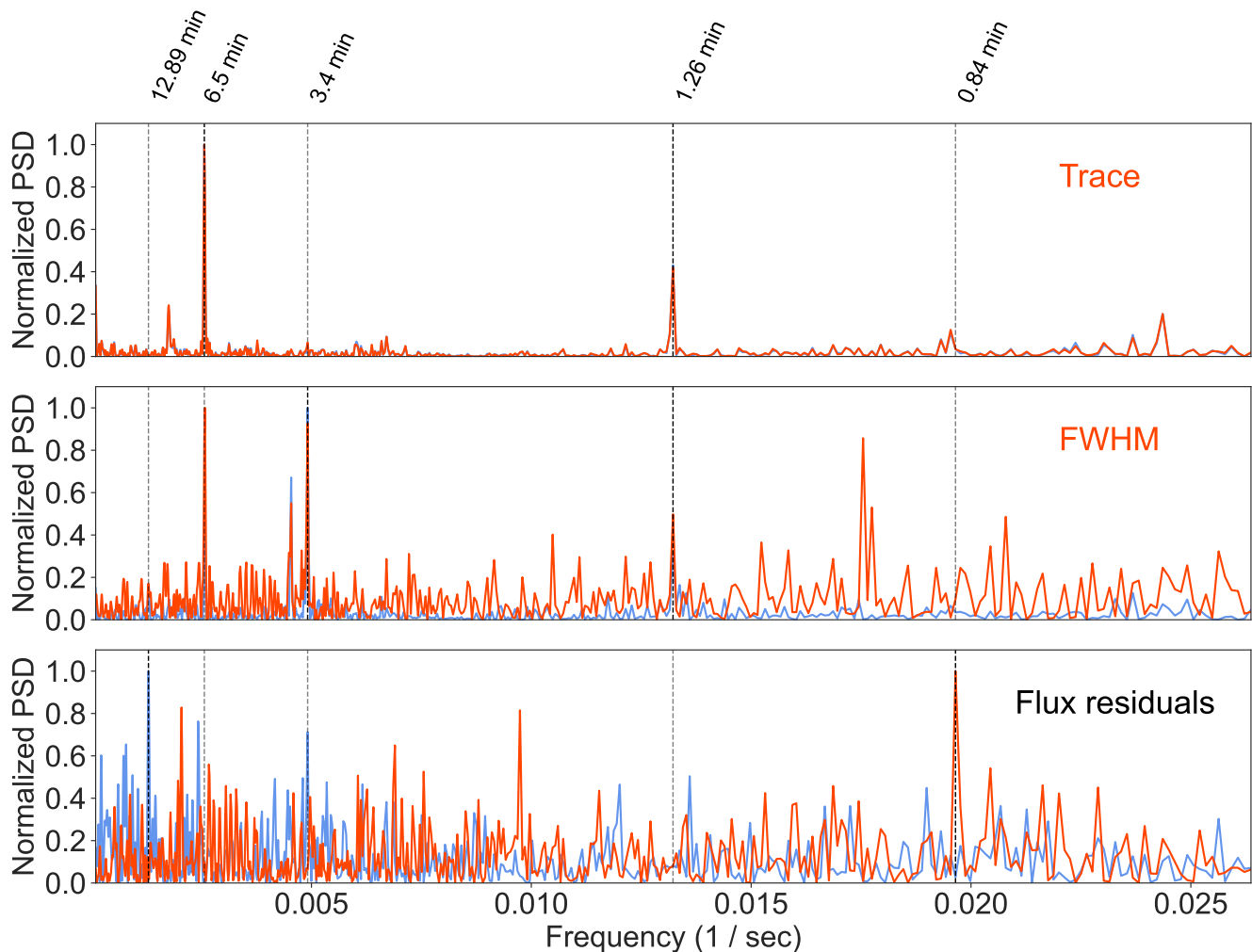


Figure 13. Power Spectral Density (PSD) of the trace (top), FWHM (middle), and band-integrated light curve flux residuals (bottom) for both the NRS1 (blue) and NRS2 (red) time-series, normalized to the highest peak. The most obvious peaks across the different PSD's are labeled with black dashed lines; the period of each of those peaks is indicated on the top panel. Note how most of the peaks in the band-integrated light curve time-series residual PSD don't really appear on the trace and the FWHM PSDs, with the exception, perhaps, of a peak at 3.4 minutes, where the FWHM also peaks. This is not a very significant peak in the band-integrated light curve PSD nonetheless (FAP > 0.1).

APPENDIX

A. PERIODOGRAM ANALYSIS OF THE TRACE, FWHM AND RESIDUAL FLUX TIME-SERIES

As shown in Figure 2, the trace position movement is consistent between the detectors, and shows the same characteristics in time: an apparent break in the position about 1.5 hours since the start of the exposure, and some high-frequency variations. These high-frequency variations are also evident from the FWHM time-series. To characterize the features in these time-series we perform a periodogram analysis on the trace position time-series, as well as the FWHM and the residuals of the band-integrated light curve fits presented in Section 2. These are presented in Figure 13.

⁶ <https://jwst.etc.stsci.edu/>

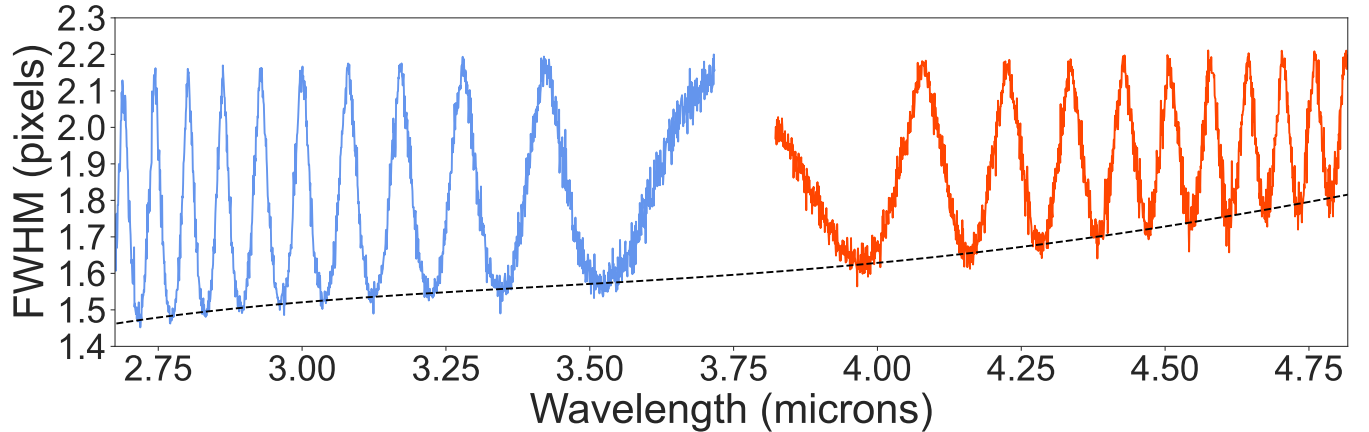


Figure 14. FWHM as a function of wavelength as measured from our G395H observations from NRS1 (left, blue) and NRS2 (right, red). Note how the FWHM quickly oscillates as a function of wavelength with an amplitude of about 0.6 pixels; we believe the oscillations are almost purely a detector sampling effect and not real variations caused by the optical elements of the G395H trace. The dashed line shows the lower envelope of this FWHM shape, which should be a good estimate of the real FWHM variation as a function of wavelength of the instrument (see text for details).

As can be seen from Figure 13, the trace and FWHM power spectral densities (PSDs) have some peaks in common. In particular, the strongest signal at 6.5-minutes appears on both periodograms. While this same peak does not directly appear in the band-integrated light curve residual PSD (bottom panel of Figure 13) a peak in the NRS1 residual lightcurve *does* show up at about twice this period (12.89 min.). The 1.26-minute peak clearly observed on the trace PSD also seems to appear on the FWHM PSD, and not at all in the band-integrated light curve flux residual PSD. The FWHM does appear to have an extra peak in the PSD at about 3.4 minutes which seems to show up in the flux residuals too, although it's not very significant in this later PSD (we measure a False Alarm Probability, FAP, for this peak of > 0.1). The time-scales of the observed peaks in the trace and FWHM periodograms all seem consistent with the time-scales of the thermal cycling of heaters in the Integrated Science Instrument Module (ISIM) onboard JWST (Rigby et al. 2022). Whether this is an actual *causal* relationship is under investigation.

B. FWHM VARIATION ACCROSS THE G395H TRACE

A notable feature to describe that was observed in our G395H observations is the evident variation of the FWHM as a function of wavelength/position in the detector, which we believe is almost purely a sampling effect. To obtain the FWHM at each position along the trace (and hence, as a function of wavelength), we fit a spline to the cross-dispersion profile, subtracting the half-maximum of this spline to itself, and then searching for the roots of it to find the FWHM. The median FWHM as a function of wavelength (obtained by obtaining the median FWHM across integrations) as measured by our G395H observations of HAT-P-14 b are presented in Figure 14.

As can be observed, the FWHM seems to vary quite rapidly throughout the detector with an amplitude of about 0.6 pixels. On average, the FWHM seems to slowly increase as a function of wavelength, with the amplitude of the modulation *decreasing* as a function of wavelength. Moreover, the lengthscale at which these modulations occur seem to decrease towards the edge of the wavelength range, being larger in the middle.

The behavior of the FWHM change across the trace is most likely a sampling effect related to the significantly tilted shape of the trace and the narrow shape of the PSF in the cross-dispersion direction, which makes the profile to be undersampled. There is ample evidence that this is the case in Figure 14 itself: the FWHM variation is much milder as a function of wavelength in the center of the wavelength range, where the trace is much less tilted than at the edges, where the variation is the strongest. We also visually inspected the cross-dispersion profiles at the peaks and valleys observed in Figure 14. There, we observed that indeed, on the peaks, where the FWHM appears to be larger, the trace position is right at the mid-point between two pixels, whereas when the FWHM appears to be smaller the trace is almost exactly positioned in the middle of a pixel.

The above suggests thus that the best measurement of the FWHM as a function of wavelength when measured with the methods outlined above would be to measure the lower envelope of our retrieved FWHM as a function of wavelength. This envelope is presented with dashed lines in Figure 14, and is a fit to the local minima of the FWHM

as a function of wavelength with a fourth degree polynomial, which we observed gave an adequate fit to them (RMS of 0.0075 pixels):

$$\text{FWHM} = c_0 + c_1\lambda + c_2\lambda^2 + c_3\lambda^3 + c_4\lambda^4,$$

with the FWHM in pixels, λ the wavelength in microns and the coefficients being $(c_0, c_1, c_2, c_3, c_4) = (-4.6210, 6.1239, -2.2736, 0.3697, -0.0216)$. This implies the FWHM evolves from about 1.52 pixels at 3 μm to about 1.85 pixels at 5 μm for G395H.

REFERENCES

- Batalha, N. E., Mandell, A., Pontoppidan, K., et al. 2017, *PASP*, 129, 064501, doi: [10.1088/1538-3873/aa65b0](https://doi.org/10.1088/1538-3873/aa65b0)
- Beichman, C., Benneke, B., Knutson, H., et al. 2014, *PASP*, 126, 1134, doi: [10.1086/679566](https://doi.org/10.1086/679566)
- Belokurov, V., Penoyre, Z., Oh, S., et al. 2020, *MNRAS*, 496, 1922, doi: [10.1093/mnras/staa1522](https://doi.org/10.1093/mnras/staa1522)
- Birkmann, S. M., Ferruit, P., Giardino, G., et al. 2022, *A&A*, 661, A83, doi: [10.1051/0004-6361/202142592](https://doi.org/10.1051/0004-6361/202142592)
- Bonomo, A. S., Desidera, S., Benatti, S., et al. 2017, *A&A*, 602, A107, doi: [10.1051/0004-6361/201629882](https://doi.org/10.1051/0004-6361/201629882)
- Brahm, R., Jordán, A., & Espinoza, N. 2017, *PASP*, 129, 034002, doi: [10.1088/1538-3873/aa5455](https://doi.org/10.1088/1538-3873/aa5455)
- Espinoza, N., & Jordán, A. 2015, *MNRAS*, 450, 1879, doi: [10.1093/mnras/stv744](https://doi.org/10.1093/mnras/stv744)
- . 2016, *MNRAS*, 457, 3573, doi: [10.1093/mnras/stw224](https://doi.org/10.1093/mnras/stw224)
- Espinoza, N., Kossakowski, D., & Brahm, R. 2019, *MNRAS*, 490, 2262, doi: [10.1093/mnras/stz2688](https://doi.org/10.1093/mnras/stz2688)
- Fukui, A., Narita, N., Kawashima, Y., et al. 2016, *ApJ*, 819, 27, doi: [10.3847/0004-637X/819/1/27](https://doi.org/10.3847/0004-637X/819/1/27)
- Giardino, G., Bhatawdekar, R., Birkmann, S. M., et al. 2022, arXiv e-prints, arXiv:2208.04876. <https://arxiv.org/abs/2208.04876>
- Howarth, I. D. 2011, *MNRAS*, 418, 1165, doi: [10.1111/j.1365-2966.2011.19568.x](https://doi.org/10.1111/j.1365-2966.2011.19568.x)
- Kipping, D. M. 2013, *MNRAS*, 435, 2152, doi: [10.1093/mnras/stt1435](https://doi.org/10.1093/mnras/stt1435)
- Kreidberg, L. 2015, *Publications of the Astronomical Society of the Pacific*, 127, 1161, doi: [10.1086/683602](https://doi.org/10.1086/683602)
- Kurucz, R. L. 1979, *ApJS*, 40, 1, doi: [10.1086/190589](https://doi.org/10.1086/190589)
- Lafreniere, D. 2017, *NIRISS Exploration of the Atmospheric diversity of Transiting exoplanets (NEAT)*, JWST Proposal. Cycle 1, ID. #1201
- Lewis, N., Clampin, M., Mountain, M., et al. 2017, *Transit Spectroscopy of TRAPPIST-1e*, JWST Proposal. Cycle 1, ID. #1331
- Lim, O., Albert, L., Artigau, E., et al. 2021, *Atmospheric reconnaissance of the TRAPPIST-1 planets*, JWST Proposal. Cycle 1, ID. #2589
- Lützendorf, N., Giardino, G., Alves de Oliveira, C., et al. 2022, in *Society of Photo-Optical Instrumentation Engineers (SPIE) Conference Series*, Vol. 12180, *Space Telescopes and Instrumentation 2022: Optical, Infrared, and Millimeter Wave*, ed. L. E. Coyle, S. Matsuura, & M. D. Perrin, 121800Y, doi: [10.1117/12.2630069](https://doi.org/10.1117/12.2630069)
- Marsh, T. R. 1989, *PASP*, 101, 1032, doi: [10.1086/132570](https://doi.org/10.1086/132570)
- Ngo, H., Knutson, H. A., Hinkley, S., et al. 2015, *ApJ*, 800, 138, doi: [10.1088/0004-637X/800/2/138](https://doi.org/10.1088/0004-637X/800/2/138)
- Patel, J. A., & Espinoza, N. 2022, *AJ*, 163, 228, doi: [10.3847/1538-3881/ac5f55](https://doi.org/10.3847/1538-3881/ac5f55)
- Pontoppidan, K. M., Pickering, T. E., Laidler, V. G., et al. 2016, in *Society of Photo-Optical Instrumentation Engineers (SPIE) Conference Series*, Vol. 9910, *Observatory Operations: Strategies, Processes, and Systems VI*, ed. A. B. Peck, R. L. Seaman, & C. R. Benn, 991016, doi: [10.1117/12.2231768](https://doi.org/10.1117/12.2231768)
- Rathcke, A., Bello-Arufe, A., Buchhave, L. A., et al. 2021, *Probing the Terrestrial Planet TRAPPIST-1c for the Presence of an Atmosphere*, JWST Proposal. Cycle 1, ID. #2420
- Rigby, J., Perrin, M., McElwain, M., et al. 2022, arXiv e-prints, arXiv:2207.05632. <https://arxiv.org/abs/2207.05632>
- Rustamkulov, Z., Sing, D. K., Liu, R., & Wang, A. 2022, *ApJL*, 928, L7, doi: [10.3847/2041-8213/ac5b6f](https://doi.org/10.3847/2041-8213/ac5b6f)
- Saha, S., & Sengupta, S. 2021, *AJ*, 162, 221, doi: [10.3847/1538-3881/ac294d](https://doi.org/10.3847/1538-3881/ac294d)
- Schlawin, E., Leisenring, J., Misselt, K., et al. 2020, *AJ*, 160, 231, doi: [10.3847/1538-3881/abb811](https://doi.org/10.3847/1538-3881/abb811)
- Simpson, E. K., Barros, S. C. C., Brown, D. J. A., et al. 2011, *AJ*, 141, 161, doi: [10.1088/0004-6256/141/5/161](https://doi.org/10.1088/0004-6256/141/5/161)
- Speagle, J. S. 2020, *MNRAS*, 493, 3132, doi: [10.1093/mnras/staa278](https://doi.org/10.1093/mnras/staa278)
- Torres, G., Bakos, G. Á., Hartman, J., et al. 2010, *ApJ*, 715, 458, doi: [10.1088/0004-637X/715/1/458](https://doi.org/10.1088/0004-637X/715/1/458)
- Zhou, Y., Apai, D., Lew, B. W. P., & Schneider, G. 2017, *AJ*, 153, 243, doi: [10.3847/1538-3881/aa6481](https://doi.org/10.3847/1538-3881/aa6481)